remote sensing

MDPI

Article

A Comprehensive Analysis of Ultraviolet Remote Sensing for Aerosol Layer Height Retrieval from Multi-Angle Polarization Satellite Measurements

Haoran Gu [1,2], Yuhuan Zhang [3,*], Cheng Fan [2], Zhengqiang Li [2,4], Weizhen Hou [2,4], Zhenhai Liu [5], Yisong Xie [2], Hua Xu [2,4], Luo Zhang [2] and Jinji Ma [1]

[1] School of Geography and Tourism, Anhui Normal University, Wuhu 241003, China
[2] State Environmental Protection Key Laboratory of Satellite Remote Sensing, Aerospace Information Research Institute, Chinese Academy of Sciences, Beijing 100101, China
[3] Satellite Application Center for Ecology and Environment, Ministry of Ecology and Environment, Beijing 100094, China
[4] University of Chinese Academy of Sciences, Beijing 100049, China
[5] Anhui Institute of Optics and Fine Mechanics, Chinese Academy of Sciences, Hefei 230031, China
* Correspondence: zhangyh@secmep.cn

Abstract: Based on the optimal estimation (OE) theory and information content analysis method, we discuss the ability to include the multi-angle satellite ultraviolet polarization channel to retrieve the aerosol layer height (ALH) for ten typical aerosol types in the China region. We also quantitatively evaluate the effects of polarization measurements and the number of viewing angles on ALH retrieval under different conditions (aerosol model, aerosol optical depth, etc.). By comparing the different degree of freedom for signal (DFS) results of ALH caused by the theoretical retrieval error changes in different microphysical parameters in the aerosol and surface model, we identify the key factors affecting ALH retrieval. The results show that the extended ultraviolet band provides important information for ALH retrieval and is closely related to the scattering and absorption characteristics of aerosol models. The polarization measurements in fine mode reduce the posterior error of ALH retrieval by 6%–39%; however, this is relatively small for coarse mode. In particular, when it is applied to the transported dust and background dust aerosol types, the posterior error is only reduced by 1%–8% after adding polarization measurements. For these two aerosol types with weak absorption at the ultraviolet band, increasing the number of angles observed in addition to increasing the polarization channel will more effectively improve ALH inversion. Compared with other aerosol and surface model parameters, the retrieval errors for the total volume column, effective variance, real part of the complex refractive index, and surface reflectance are the main factors affecting ALH retrieval. Therefore, reducing the theoretical retrieval error of these parameters will be helpful.

Keywords: Information Content Analysis; aerosol layer height; optimal estimation inversion; multiangle polarimetric remote sensing; a posteriori error

Citation: Gu, H.; Zhang, Y.; Fan, C.; Li, Z.; Hou, W.; Liu, Z.; Xie, Y.; Xu, H.; Zhang, L.; Ma, J. A Comprehensive Analysis of Ultraviolet Remote Sensing for Aerosol Layer Height Retrieval from Multi-Angle Polarization Satellite Measurements. *Remote Sens.* **2022**, *14*, 6258. https://doi.org/10.3390/rs14246258

Academic Editor: Tamas Várnai

Received: 6 November 2022
Accepted: 8 December 2022
Published: 10 December 2022

1. Introduction

Aerosols are liquid or solid particles suspended in gas with a certain level of stability that have significant impacts on the global radiative energy balance and climate change. The aerosol vertical distribution is an important parameter associated with the retrieval of highly precise aerosol microphysical properties (a previous study has shown the spectral dependence of the radiation effect on the aerosol layer height) that plays an important role in the study of radiative forcing [1]. For example, it is necessary to consider aerosol scattering in trace gas and ocean color retrieval and modify the aerosol vertical

distribution parameters accordingly [2–4]. The aerosol layer height (ALH) is a major determining factor in the passive remote sensing monitoring of atmospheric fine particulate matter, such as $PM_{2.5}$, near the ground. One such approach is the spaceborne $PM_{2.5}$ remote sensing method (PMRS) [5,6]. ALH is commonly used in model calculation, while in the passive remote sensing measurements, it can be always be replaced by planetary boundary layer height (PBLH). The planetary boundary layer is the lowest layer of the atmosphere and, which contains the vast majority of aerosols of the low troposphere [6,7]. At the same time, the height information on smoke, volcanic, and dust aerosols can provide the initial conditions for the modeling of their emissions and the physics of plume formation [8–10]. Consequently, it is imperative to observe the vertical distribution of aerosols on a global scale in order to validate transport models and better understand the impact of aerosols on the climate and environment of the Earth [10,11].

Satellite remote sensing offers the possibility of measuring aerosol height information on a global scale. Active remote sensing measurements, such as ground-based, flight-based, and space-based measurements, can effectively measure the vertical distribution of aerosols. For instance, Cloud-Aerosol Lidar with Orthogonal Polarization (CALIOP) can measure the backscatter at each vertical layer, resulting in detailed aerosol extinction coefficient profiles based on the backscatter ratio [12]. Passive remote sensing measurements, while not having the same accuracy or resolution as active remote sensing, can provide considerable spatial coverage and higher temporal resolution by using ultraviolet (UV), visible/near infrared (VNIR), and thermal infrared (TIR) band observations [10]. In passive remote sensing, most studies focus on the O_2 A band [12–14]. Comprehensive studies have shown that the vertical distribution of oxygen absorption bands is generally stable and not affected by the emissions [13], which is one of the important ways to retrieve ALH. In practice, it is challenging to reach an agreement between the retrieved aerosol height from real O_2 A band measurements and LIDAR measurements, which depend on ad hoc assumptions. Often, higher spectral resolution sensors are used or, given the advantage of reducing interference from the surface, measurements are combined with the O_2 B band to improve the retrieval accuracy [14]. The stereoscopic technique, which relies on the principle of parallax, is applicable for the retrieval of plume-type aerosols with discernable textures, while it is not affected by complex aerosol microphysical properties and radiative transfer computation [15,16].

Applying the UV-A band (315-400nm) is another approach for ALH passive retrieval, because in the ultraviolet and near-ultraviolet bands, the elevated aerosol layer partly shields the polarization signal from Rayleigh scattering, providing sensitivity to the aerosol layer height [17,18]. On the other hand, the aerosol information will be improved when the surface albedo decreases, and the lower surface reflectance in the UV wavelength is also beneficial for the retrieval of ALH. A previous study performed retrievals with Research Scanning Polarimeter (RSP) measurements in the near-ultraviolet and blue spectral bands. The validation against measurements from a CALIOP showed good agreement with an absolute ALH difference of less than 1 km. The study also indicates the possibility for future satellite instruments to better retrieve aerosol height information if they may include wavelengths shorter than 410 nm [10]. There are some existing sensors that already include polarization channels in the single-angle UV band, such as the Ozone Monitoring Instrument (OMI) [19], Particulate Observing Scanning Polarization (POSP), and so on [20]. However, there is a lack of evidence that multi-angle polarization measurements are better for ALH inversion in UV than near UV. More and more multi-angle polarized instruments are being launched in China for remote sensing studies of atmospheric aerosol properties [21–24]. Since the inversion of the aerosol layer height in the UV band often requires additional constraints, the aerosol model should be assumed in the inversion algorithm in advance, which may introduce errors [25]. Multi-angle polarization provides just enough observational information to improve the accuracy of the inversion.

In this paper, we focus on the typical aerosol types in China and further quantitatively investigate the influence of multi-angle polarization measurements on the retrieval

of ALH based on these models. The aim of this study is to determine whether the multi-angle polarization measurements of the UV band can provide enough information to retrieve ALH and to investigate how UV multi-angle polarization observations can be used for remote sensing inversion of ALH of different aerosol types. We also demonstrate the influence of aerosol and surface model parameter errors by the degree of freedom for signal (DFS) of ALH retrieval under different conditions (aerosol loads, model types, multi viewing observation and so on). The results of this study could be used to develop the next generation spaceborne polarimetric sensors and corresponding ALH retrieval algorithms.

2. Materials and Methods

2.1. Optimal Estimation Theory

Following the optimal estimation (OE) theory [26], ALH retrieval is the process of obtaining the best matching ALH parameter based on satellite observations. The forward model can be described as

$$\boldsymbol{y} = F\left(\boldsymbol{x},\ \ \boldsymbol{b}\right) + \epsilon \tag{1}$$

where $\boldsymbol{x}$ is a state vector, $\boldsymbol{b}$ comprises parameters that are not present in $\boldsymbol{x}$ but have a quantitative impact on TOA measurements, $\boldsymbol{y}$ is an observation vector, F is a forward model, and $\boldsymbol{\epsilon}$ represents an experimental error term that integrates observation noise and forward model uncertainty.

Meanwhile, the maximum likelihood analysis of $\boldsymbol{x}$ can be described as

$$\hat{\boldsymbol{x}} = \boldsymbol{x}_{\mathrm{a}} + \left(\boldsymbol{K}^{\mathrm{T}}\boldsymbol{S}_{\epsilon}^{-1}\boldsymbol{K} + \boldsymbol{S}_{\mathrm{a}}^{-1}\right)^{-1}\boldsymbol{K}^{\mathrm{T}}\boldsymbol{S}_{\epsilon}^{-1}(\boldsymbol{y} - \boldsymbol{K}\boldsymbol{x}_{\mathrm{a}}) \tag{2}$$

where the superscript "−1" is the inverse operation of the matrix, $\boldsymbol{S}_{\mathrm{a}}$ is the error covariance matrix of the a priori estimate $\boldsymbol{x}_{\mathrm{a}}$, and $\boldsymbol{K}$ is the Jacobian matrix, which consists of the partial derivatives of $\boldsymbol{F}(\mathbf{x})$ with respect to $\boldsymbol{x}$ and describes the sensitivity of the forward model to the state vector. $\boldsymbol{S}_{\epsilon}$ is the covariance matrix of the error. The a priori estimate provides constraints for the retrieval of the optimal estimation algorithm to prevent the generation of unreasonable results.

In Equation (2), $\hat{\boldsymbol{x}}$ corresponds to the minimum value of the scalar-valued cost function after convergence, and the scalar-valued cost function $\boldsymbol{J}$ is used as the form of

$$\boldsymbol{J} = (\boldsymbol{y} - \boldsymbol{K}\boldsymbol{x})^{\mathrm{T}}\boldsymbol{S}_{\epsilon}^{-1}(\boldsymbol{y} - \boldsymbol{K}\boldsymbol{x}) + (\boldsymbol{x} - \boldsymbol{x}_{\mathrm{a}})^{\mathrm{T}}\boldsymbol{S}_{\mathrm{a}}^{-1}(\boldsymbol{x} - \boldsymbol{x}_{\mathrm{a}}) \tag{3}$$

The posteriori error is also known as the theoretical retrieval error. It can be calculated by combining the prior error with error propagation, which can be written as

$$\hat{\boldsymbol{S}} = \left(\boldsymbol{S}_{\mathrm{a}}^{-1} + \boldsymbol{K}^{\mathrm{T}}\boldsymbol{S}_{\epsilon}^{-1}\boldsymbol{K}\right)^{-1} \tag{4}$$

This indicates that the statistical uncertainties in retrieved $\hat{\boldsymbol{x}}$ due to noise in measurements and error propagation, as well as the posterior errors (absolute errors), are equal to the square root of the diagonal elements.

Besides the posterior error covariance matrix, another key parameter that measures the amount of information about the parameters recovered from observations is the averaging kernel function $\boldsymbol{A}$:

$$\boldsymbol{A} = \frac{\partial \hat{\boldsymbol{x}}}{\partial \boldsymbol{x}} = \left(\boldsymbol{K}^{\mathrm{T}}\boldsymbol{S}_{\epsilon}^{-1}\boldsymbol{K} + \boldsymbol{S}_{\mathrm{a}}^{-1}\right)^{-1}\boldsymbol{K}^{\mathrm{T}}\boldsymbol{S}_{\epsilon}^{-1}\boldsymbol{K} \tag{5}$$

The degree of freedom for signal (DFS), also known as the trace of the averaging kernel matrix $\boldsymbol{A}$, denotes the amount of information about the retrieved parameters that can be explored from the satellite data. When the matrix is the identity matrix, the retrieved state can fully reflect the true state; Typically, we may assume that the parameter

can be retrieved when the DFS result is >0.5 [27,28]. Each diagonal element, in turn, describes the information contained in each retrieved parameter, given that the averaging kernel specifies the relative weight of information about the state vector contained in satellite measurements as well as from a priori measurements [29]. Considering that the averaging kernel describes the relative weight of information about the state vector from the satellite measurements compared with that from the a priori measurements, the DFS value depends on the a priori uncertainty assumption. In other words, a higher "degree of freedom for signal" corresponds to a lower posterior error with the same a priori measurement. Therefore, in this work, we quantified the ALH information supplied by UV band satellite data by comparing the posterior uncertainty to the prior uncertainty. The model simulates the Jacobians of the retrieved and supplementary parameters ($\boldsymbol{K}$ and $\boldsymbol{K}_b$), whereas the error covariance matrices are determined empirically (Section 3.2.3).

2.2. Radiative Transfer Simulation

The Unified Linearized Vector Radiative Transfer Model (UNL-VRTM) is used to simulate satellite observations and related weighting functions regarding parameters retrieved for multi-angle viewing geometries. For UNL-VRTM to simulate TOA reflectance and polarization, the sensor setup, atmospheric profile, aerosol characteristics, and surface reflectance are also required as inputs. The vertical profiles of atmospheric temperature, pressure, and trace gases are presumed to be based on the mid-latitude summer atmospheric profiles from Optical Properties of the Atmosphere, Third Edition, AFCRL-72-0497. The 49-layer standard atmospheric profile is mapped to the GEOS-5 vertical grids with 47 hybrid pressure-sigma layers to increase the vertical resolution [30]. Meanwhile, the MT CKD model created by Mlawer, D.C. Tobin, and S.A. Clough is used to determine the continuum absorption of water vapor [31]. The UNL-VRTM is based on the VLIDORT model for calculating the Stokes vector $\left[I,\ Q,\ U,\ V\right]^T$, and details about each module in UNL-VRTM can be found in [32], where I represents the total radiant intensity, Q represents the difference between the linearly polarized components parallel to and perpendicular to the reference plane, U describes the linearly polarized irradiance on the polarization plane at an angle of ±45° from the reference plane, and V describes the circular polarization. We consider an observation vector comprising I and the degree of linear polarization (*DoLP*) which can eliminate the influence of absolute calibration, where *DoLP* is defined by

$$DoLP = \frac{\sqrt{Q^2 + U^2}}{I} \tag{6}$$

Furthermore, the Jacobian matrix of the *DoLP* for each component of the state vector can be described as

$$\frac{\partial DoLP}{\partial x} = -\frac{DoLP\dfrac{\partial I}{\partial x_i}}{I} + \frac{Q\dfrac{\partial Q}{\partial x_i} + U\dfrac{\partial U}{\partial x_i}}{I\sqrt{Q^2 + U^2}} \tag{7}$$

Using the superscripts v_1–v_M to note each viewing in multiple observations, the measurement vector y can be described as

$$y = \left[I_\lambda^{v_1}, ..., I_\lambda^{v_M}, DOLP_\lambda^{v_1}, ..., DOLP_\lambda^{v_M} \right]^T \tag{8}$$

The Jacobian matrix calculation of $\boldsymbol{y}$ to $\boldsymbol{x}$ is performed by the UNL-VRTM. Combined with the simulated propagation of errors and the posterior errors, DFS and a posterior error of ALH under different aerosol types and observed geometry can be derived from Equations (4) and (5). According to the results, we can carry out the sensitivity analysis.

3. Instrument and Simulation Assumptions

3.1. Observation Geometry Setting

The instrument in this study is a pre-developed sensor with extra capacity to measure polarization at multi-angle observations in the UV band. We refer to it as Multi-Angle Polarization Measurements with Ultraviolet band (MAPMU). Microphysical and optical properties of aerosols are derived from multi-angle measurements in 11 spectral bands from 388 to 2140 nm with bands near 388, 490, 670, 865, 1370,1640, and 2140 nm performing polarimetric measurements in addition to radiance. The properties of MAPMU are listed in Table 1 and the fundamental simulation presumptions, such as the aerosol model, the surface model, and the error covariance matrix, are discussed in this part.

Table 1. Basic characteristics of MAPMU.

Parameter	Value	Parameter	Value
Spatial res. (m)	500 (vertical resolution)	Multi-angle	5
Instrument FOV	±45°	Polarized angle	0°, 60°,120°
Pol. Cal. Error	≤2%	Stokes parameters	I, Q, U
Rad. Cal. Error	≤5%	Band width (nm)	20, 20, 20, 20, 10, 40, 20, 40, 40, 40, 40
Central wavelength/nm	388 (P), 443, 490 (P), 670 (P), 555, 865 (P), 910, 1045, 1370 (P), 1640 (P), 2140 (P)		

Four multi-viewing observation geometries were taken into consideration with the combinations of various solar zenith angles (θ_0), viewing zenith angles (θ_v), and relative azimuth angles (φ) to represent the typical observations in various locations in order to obtain synthetic MAPMU data for the information content analysis, just as listed in Table 2. Here, summer low and summer high refer to observations at low and high solar zenith angles, respectively. Figure 1a shows the polar-plot observational geometries, in which the radius means the θ_v change from 0° to 60° with steps of 20°, and the circle represents the change in φ from 0° to 360°. Correspondingly, Figure 1b plots the scattering angles based on the observational geometries within the ranges of [137.76°, 173.68°], [105.05°, 121.30°], [80.28°, 109.40°], and [104.04°, 145.82°].

Table 2. Multi-viewing observation geometries for forward simulations (corresponding to Figure 1).

Geometry Scenarios	Solar Zenith Range (°)	Viewing Zenith Range (°)	Relative Azimuth Range (°)	Scattering Angle Range (°)
Geometry 1	54.12~54.79	44.39~64.09	5.78~330.03	137.76~173.68
Geometry 2	32.86~33.59	25.59~58.64	106.99~248.41	105.05~121.30
Geometry 3	53.18~53.74	28.8~61.06	97.15~229.85	80.28~109.40
Geometry 4	77.63~78.08	37.15~61.87	0.65~298.07	104.04~145.82

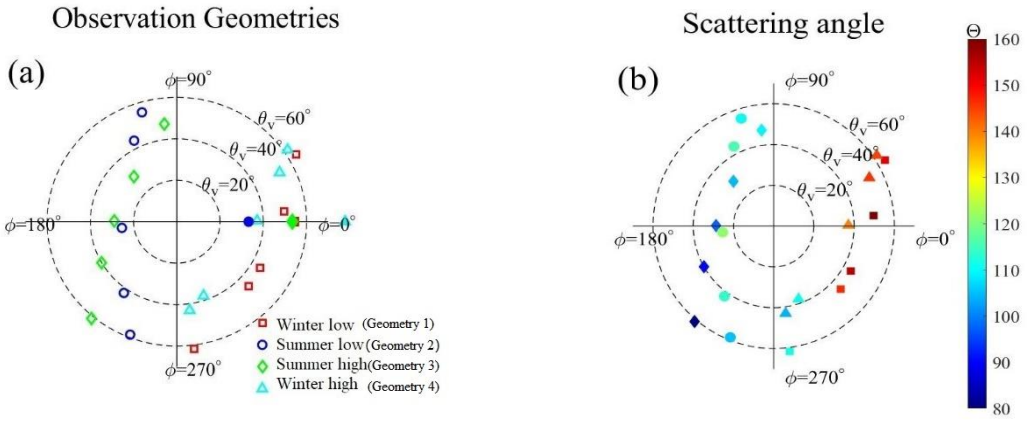

Figure 1. Observation geometries (a) with its corresponding scatter angle (b) of MAPMU sensor adopted in the simulation. In panel (**a**), the different geometries with φ = 0° represent the corresponding positions of the sun for summer low, summer high, winter low, and winter high scenarios, respectively.

3.2. Simulation Assumptions

3.2.1. Aerosol Model

The optical and microphysical characteristics of global aerosols vary greatly throughout both space and time. The climatic variables that control their removal and transport processes have significant impacts on their vertical and horizontal dispersion. There is a large range of values for the optical and microphysical characteristics of different forms of aerosol [33]. A theoretical analysis employing every form of aerosol is a difficult and unrealistic method. In order to simplify this method, previous studies have often analyzed some typical aerosol types (such as fine-dominated and coarse-dominated types) [7,28,34]. We hope to use a more realistic aerosol model classification while building a more sophisticated ALH retrieval framework for the Chinese region in order to explore the ability of UV multi-angle polarization measurements to undergo ALH retrieval for different aerosol types.

Based on the ground-based remote sensing measurements of the Sun-sky radiometer Observation NETwork (SONET), ten fundamental aerosol models used in China were derived in a cluster study by Li et al., and the classifications are summarized in Table 3 [35].

The ten clusters suggest five typical fine particle aerosol models and five coarse models, including urban polluted, secondary polluted, combined polluted, polluted fly ash, and continental background, summer fly ash, winter fly ash, primary dust, transported dust, and background dust. Table 4 lists the details of the microphysical parameters, including the total aerosol volume (V_0)、effective radius (r_{eff}) and variance (v_{eff}) as well as the refractive index, as shown in the results in Figure 2. In the fine-particle size range, there are five single-peak aerosol models (F-ULW, F-UHS, C-ULW, C-UHS, and C-UNW) and five double-peak (F-BLW, F-BNS, F-BNM, C-BNM and C-BHM) aerosol models. It should be noted that the double-peak feature may not be obvious, because one small peak may be covered by another big peak [35].

Table 3. Aerosol model classification with SONET [35].

Mode	Aerosol Type	Description of characteristics
Fine Mode	Urban polluted (F-ULW)	Urban-polluted fine-mode aerosols with high particle concentrations
	Continental background (F-UHS)	Background fine-mode aerosols with low particle concentrations
	Secondary polluted (F-BLW)	Secondary aerosols containing mainly polluted particles with low refractivity and a higher scattering capacity
	Combined polluted (F-BNS)	Mixture of direct anthropogenic emissions and secondary aerosols with high light absorption
	Polluted fly ash (F-BNM)	Mixture of anthropogenic-polluted particles and fine fly ash particles with large submicron fine particles
Coarse Mode	Summer fly ash (C-ULW)	Background of fly ash coarse particles with low light absorption, for example, natural emissions of primary organic aerosols
	Winter fly ash (C-UHS)	Background of fly ash coarse particles with high light absorption, for example, fly ash polluted by anthropogenic components
	Primary dust (C-UNW)	Coarse particles of natural dust with a very high volume concentration
	Transported dust (C-BNM)	Dust particles after long-term transportation and sedimentation
	Background dust (C-BHM)	Background dust suspended over continental regions with a large coarse standard mode

Table 4. Microphysical parameters of ten typical aerosol models in China.

Fine Modes									
Type	r_{eff}	r_{eff}^{sm}	v_{eff}	v_{eff}^{sm}	Refractive Index	V_0	V_0^{sm}	Refractivity	Absorptivity
F-ULW	0.175	\	0.300	\	1.414-0.007i	0.136	\	Low	Weak
F-UHS	0.126	\	0.334	\	1.515-0.014i	0.063	\	High	Strong
F-BLW	0.132	0.283	0.152	0.257	1.392-0.007i	0.087	0.069	Low	Weak
F-BNS	0.103	0.204	0.089	0.334	1.459-0.016i	0.046	0.089	Normal	Strong
F-BNM	0.124	0.387	0.189	1.766	1.477-0.011i	0.073	0.058	Normal	Moderate
Coarse Modes									
C-ULW	2.208	\	0.522	\	1.437-0.006i	0.089	\	Low	Weak
C-UHS	2.558	\	0.500	\	1.522-0.015i	0.090	\	High	Strong
C-UNW	1.970	\	0.305	\	1.495-0.003i	0.482	\	Normal	Weak
C-BNM	1.211	2.973	0.345	0.552	1.492-0.009i	0.059	0.105	Normal	Moderate
C-BHM	1.626	4.481	0.552	0.142	1.518-0.008i	0.121	0.076	High	Moderate

V_0 is the total aerosol volume ($\mu m^3/\mu m^2$), The subscript sm is for the submicron fine mode or supermicron coarse mode.

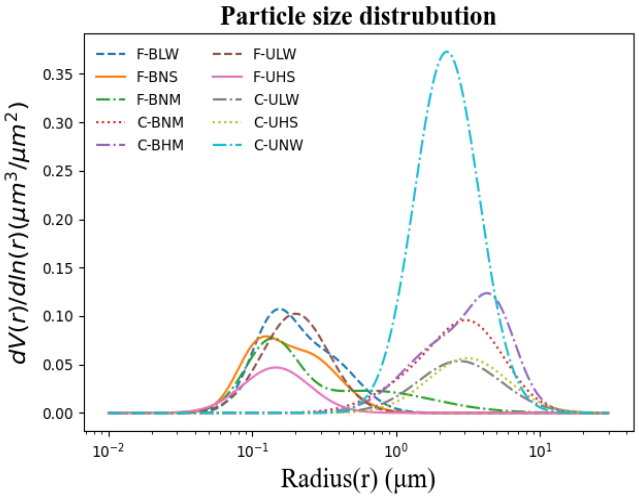

Figure 2. The aerosol volume size distributions for the ten aerosol types defined in Table 4.

The scattering phase matrix $\boldsymbol{P}$ is simulated using a linearized Mie code once these microphysical characteristics have been input:

$$\boldsymbol{P} = \begin{bmatrix} P_{11} & P_{12} & 0 & 0 \\ P_{21} & P_{22} & 0 & 0 \\ 0 & 0 & P_{33} & P_{34} \\ 0 & 0 & P_{43} & P_{44} \end{bmatrix} \quad (9)$$

where $P_{12} = P_2$ and $P_{34} = P_{43}$. P_{11} is the normalized phase function that describes the scalar component of particle scattering, whereas $-P_{12}/P_{11}$ is the polarized scattering that corresponds to DoLP.

The single scattering albedo (SSA) in the UV and VIS bands for ten typical aerosol models is also shown in Table 5. SSA represents the ratio of the scattering efficiency to the total extinction efficiency. Compared with the VIS band (443 nm), the SSA in the UV band is higher for the fine mode, while the SSA of the coarse mode is lower.

Table 5 indicates stronger absorption for F-ULW, F-BNS, and F-BNS compared to F-BLW and F-BNM. Similarly, weaker absorption is shown for C-BNM and C-BHM compared to C-ULW, C-UHS, and C-UNW for the wavelength at 388 nm.

Table 5. SSA of ten aerosol models at 338 nm and 443 nm.

SSA	F-BLW	F-BNS	F-NM	F-ULW	F-UHS	C-ULW	C-BNM	C-BHM	C-UHS	C-UNW
SSA (388 nm)	0.9541	0.9020	0.9572	0.9277	0.9413	0.7642	0.7906	0.7666	0.6194	0.6338
SSA (443 nm)	0.9498	0.8895	0.9569	0.9261	0.9377	0.7817	0.8082	0.7842	0.6333	0.6496

The wavelength-dependent P_{11} and $-P_{12}/P_{11}$ of various aerosol types vary with different scattering angles, as shown in Figure 3a,b,c,d resulting in diverse scattering properties that impact TOA measurements. Figure 3c,d additionally show four multi-viewing observation geometries with varying sensitivities to TOA radiance and DoLP with respect to ALH. As an example, when the scattering angle gradually moves closer to 180°, the aerosol DoLP ($-P_{12}/P_{11}$) with scattering angles for C-BHM and C-BNM is obviously different from the other three coarse aerosol models, and the overall value is negative. This bimodal aerosol model has the characteristics of Asia dust and transport dust. Due to the high aerosol layer and special optical characteristics of the UV band, the absorption is weak.

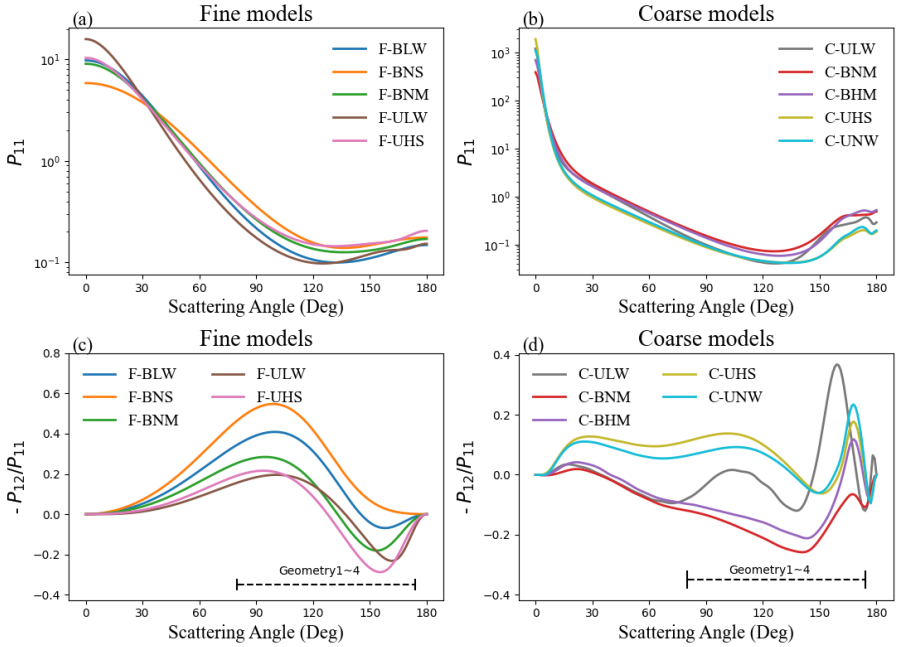

Figure 3. Scattering phase functions (a,b) and polarized phase functions (c,d) of ten typical aerosol models at a wavelength of 388 nm. (a,c) represents fine mode aerosol types and (b,d) represents coarse mode aerosol types.

From the perspective of passive remote sensing, we assume that only one aerosol layer is present in the atmosphere, and the definition of the aerosol height depends on how the profile is represented. Meanwhile, the suitable choice of representation often depends on the actual applications. It also depends on whether the measurement can meet the profile model parameters which are in the state vectors to solve at the same time. In the simulation, we assume that the profile of the aerosol extinction coefficient follows an exponential-decay profile, which is often used in atmospheric correction algorithms and can be written in the form of [7,32,36]:

$$\int_{TOA}^{Z} \tau(z)\,dz = \tau_0 \exp\left(-\frac{z}{H}\right) \tag{10}$$

where τ_0 is the columnar aerosol optical depth (AOD), and H is the scale height, which represents the height of the aerosol layer when the columnar aerosol optical depth (AOD) decays to 1/e of the ground. To simplify this, we only include H in our retrieval's state vector, while the other aerosol-related characteristics (AOD, effective radius, variance, and refractive index) are specified as model parameters.

3.2.2. Surface Model

The surface reflectance has a significant impact on ALH information; hence, it is vital to choose the proper surface reflectance model. Many studies have suggested that compared with bare soil (bright surface case), surface types with relatively higher absorption (seawater, vegetation, etc.) show higher sensitivity to the ALH [1,29]. However, the surface reflectance of different types is relatively low at the UV band, and the difference is small. For instance, we use the improved kernel-driven bidirectional reflectance distribution function (BRDF) model of vegetated surface, which has been proven to provide a better retrieval performance than the traditional Ross-Li model in the multi-angle polarization satellite observation retrieval framework [37]. For surface reflectance, the used BRDF is

$$\rho_S(\mu_0,\mu_v,\phi,\lambda) = f_{iso}(\lambda)[1 + k_1 f_{geom}(\mu_0,\mu_v,\phi) + k_2 f_{vol}(\mu_0,\mu_v,\phi)] \quad (11)$$

where μ_0 and μ_v represent the cosine of the solar zenith angles and the viewing zenith angle, respectively; f_{iso}, f_{geom}, and f_{vol} correspond to the isotropic, geometric-optical (Li-sparse kernel), and volumetric (Ross-thick kernel) surface scattering, respectively. k_1 and k_2 are the coefficients of the BRDF kernels at the given wavelength. In this paper, the surface reflectance f_{iso} was set to 0.0186, a value chosen from the surface reflectance databases USGS and ASTER[38,39]. The values of k_1 and k_2 were chosen from Litvinov's work as equal to 0.087 and 0.668 [40].

3.2.3. Error Covariance Matrix

As described in Section 2, we constructed the inversion framework as described in [10]. The state vector has only one parameter, which is

$$\boldsymbol{x} = [H]^T \quad (12)$$

At the same time, the other aerosol model surface parameters were retrieved from other satellite channels with certain retrieval errors under the known inversion framework. For the double-peak aerosol models, the vector is

$$\boldsymbol{b} = \left[V_0, V_0^{sm}, r_{\mathit{eff}}, r_{\mathit{eff}}^{sm}, v_{\mathit{eff}}, v_{\mathit{eff}}^{sm}, m_r, m_i, m_r^{sm}, m_i^{sm}, \rho_s, k_1, k_2\right]^T \quad (13)$$

where V_0 and V_0^{sm}, r_{eff} and r_{eff}^{sm}, v_{eff} and v_{eff}^{sm}, m_{r} and m_{r}^{sm}, m_{i} and m_{i}^{sm} correspond to the total aerosol volume, effective radius, variance, as well as the real and imaginary parts of the refractive index in fine-mode (coarse-mode) or submicron fine mode (super-micron coarse mode); ρ_s, k_1, k_2 are the improved BRDF model parameters.

For the error covariance matrix, here, we assume that $\sigma H = 75\%H$ and the prior error covariance matrix is an identity matrix.

$$\boldsymbol{S}_a = \left[\sigma_H^2\right], \quad (14)$$

The prior error is 20% for V_0^f and V_0^{sm}, and 10% for ρ_s. For the fine-mode, the a priori errors r_{eff}, v_{eff}, m_{r}, m_{i}, k_1, and k_2 are 15%, 15%, 0.025, 50%, 15%, and 15%, respectively, while for the coarse-mode, the a priori errors r_{eff}, v_{eff}, m_{r}, m_{i}, k_1, and k_2 are 35%, 35%, 0.04, 50%, 35%, and 35%, respectively. Here, the a priori error refers to the retrieval errors of SONET [41,42]. The diagonal error covariance matrix of $\boldsymbol{b}$ (S_b) is

$$\boldsymbol{S}_b = \mathrm{diag}\left(\left[\left(\Delta V_0\right)^2, \left(\Delta V_0^{sm}\right)^2, ..., \left(\Delta m_i^{sm}\right)^2, \left(\Delta \rho_s\right)^2, ..., \left(\Delta k_2\right)^2\right]\right) \quad (15)$$

The uncertainties of satellite measurements ($\boldsymbol{S}_{\mathrm{y}}$), as part of the observation uncertainty, include systematic and random errors that occur during the instrument observation process. For the MAPMU instrument, we estimated radiance and polarized measurement errors of 5% and 2%, respectively. The correlations of observations between multiple viewing angles should be considered in multi-angle satellite observations, but polarization and intensity measurements can still be assumed to be independent. Therefore, $\boldsymbol{S}_{\mathrm{y}}$ is a 10 × 10 off-diagonal matrix, and the details of the construction are shown in Equation (A1).

4. Results

4.1. Simulated TOA Results

To provide synthetic data from the MAPMU measurements, we defined the TOA reflectance (R^{TOA}) and polarized reflectance (R_P^{TOA}) as follows. All of the synthetic data were cloud free.

$$\begin{cases} R^{TOA} = \pi I / \mu_0 \\ R_P^{TOA} = \pi\sqrt{Q^2 + U^2} / \mu_0 \end{cases} \quad (16)$$

Figure 4 illustrates the TOA normalized radiance and polarized radiance of different multi-viewing observation geometries at 388 nm for the F-ULW and C-ULW aerosol types. These two models (coappearance probability greater than 5%) also represent aerosol characteristics in the China region. TOA measurements for the other seven aerosol types are not shown in the figures for simplicity, although the characteristics are similar.

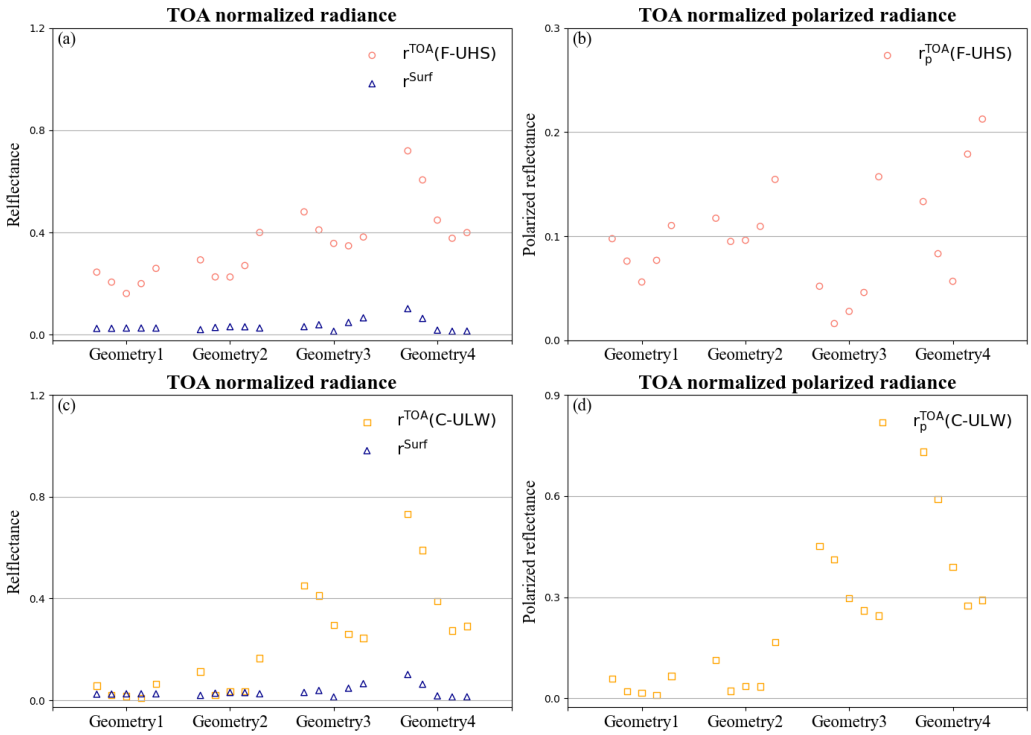

Figure 4. Contributions of TOA reflectance and TOA polarized reflectance at 388 nm with vegetated surface, and AOD = 0.6 at 550 nm. (**a**,b) correspond to the F-UHS aerosol type, while (c,d) correspond to the C-ULW aerosol type.

4.2. ALH Retrieval Capability for Typical Cases

In this section, we analyze the ability of MAPMU to detect ALH in the UV band. Four multi-angle observation geometries were used for the forward simulations, and each mean DFS of the observation geometries was calculated under the conditions of AOD = 0.6 (550 nm) and H = 2 km. Figure 5 further illustrates the DFS and posterior errors of ALH retrieval for different aerosol models in the form of histograms, and the error bars correspond to four multi-viewing observation geometries. The gray bottom column represents the prior estimation error for the aerosol layer height, and the visible part of the gray bottom column shows the reduction in the posterior error relative to the prior error in Figure 5c,d (absolute a priori error is 1.5 km).

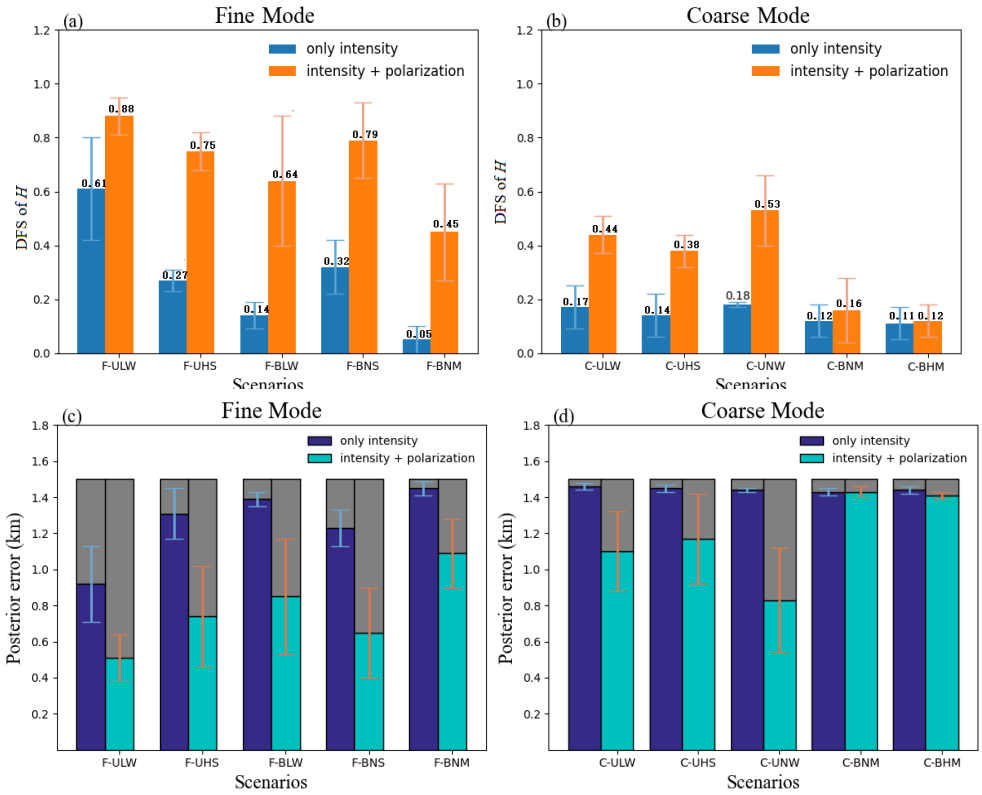

Figure 5. The DFS and posterior error of *H* for different aerosol models with AOD = 0.6 for two aerosol types over vegetation surfaces. The error bar are the mean value and standard deviation of different geometries and the aerosol profile H is defined as 2 km. (**a**,**c**) represents fine mode aerosol types and (**b**,**d**) represents coarse mode aerosol types.

(1) The results show that the multi-angle polarization measurements of ALH retrieval performed well (DFS > 0.5) in the UV band for the main aerosol models. Previous studies have shown that the surface reflectance on the information content of ALH often has more impact than the optical aerosol properties [29]. It can be seen that the optical properties of aerosols also play crucial roles in ultraviolet ALH retrieval.

(2) The determination of ALH for the coarse mode is relatively difficult compared with the fine mode, and the information content of ALH is closely related to the scattering and absorption characteristics of the aerosol model. Combined with the aerosol model SSA presented in Section 3.2.1, the fly ash pollution type (F-BNM) has the strongest scattering characteristics in the five fine modes, as a result of having the lowest DFS result, which is even lower than that found for some coarse modes. Similarly, the difference between the primary dust type (C-UNW) with the highest DFS and background dust with the lowest DFS is 0.07, and the difference grew further to above 0.4 after adding the polarization measurements. The result also indicates a better performance of the MAPMU observations for absorbing aerosol in ALH retrieval.

(3) Comparing intensity observation and polarization observation, it can be seen that, regardless of the type of aerosol (except F-ULW), it is difficult to retrieve the scale height parameter using only the intensity observation in the UV band, and the addition of polarization observation information effectively improves ALH retrieval. We supplement and test the information related to ALH retrieval under different aerosol conditions in Section 5.1 and evaluate the improvement produced by adding polarization measurements.

(4) As shown in Figure 5c,d, due to the different aerosol models, when only the intensity measurements are included, the posterior error for fine mode is in the range of 1.45

km to 0.92 km; however, once polarization measurements are included, the posterior error can drop to a range of 1.09 km to 0.51 km. For Coarse mode, the posterior error is in the range of 1.46 km to 1.43 km when just intensity measurements are used, while it is in the range of 1.43 km to 0.62 km when polarization measurements are added. In summary, the DFS of the ALH is significantly improved with the addition polarization measurements, and the posterior error is gradually reduced.

In addition, we assume that if the wrong aerosol model is chosen, the theoretical error due to the intensity and polarization measurement model choice can be quantitatively assessed by calculating the relative error of the posterior error between different models. As results shown in Figure 6, in extreme cases, the aerosol model used for the actual intensity measurement is the urban pollution type (F-ULW), but we chose the background dust type (C-BHM) for ALH inversion. The absolute error corresponding to the posterior error of the two models is, at most, 59.1%. After adding the polarization measurement, the difference between different models increases further and can reach 180.39%. That is to say, the uncertainty of the aerosol model has an important impact on ALH retrieval.

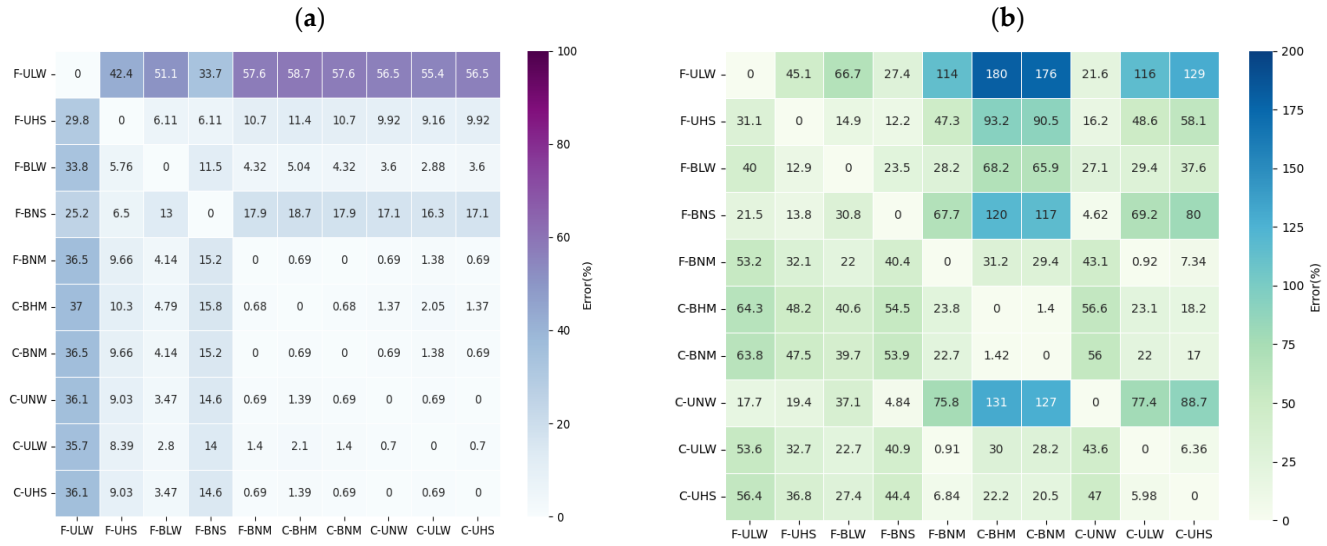

Figure 6. Heat maps of the absolute error corresponding to the posterior error caused by inaccurate aerosol models. (**a**) represents intensity measurements only; (**b**) represents "intensity + polarization" multi-angle measurements.

5. Discussion

5.1. The Influence of Adding Polarization Measurements

In Section 4.2, we analyze the ability of MAPMU to detect the aerosol layer height for typical cases and show the impact of uncertainty for aerosol models. However, previous studies have shown that the aerosol vertical distribution is also affected by the aerosol model parameters (AOD, H), while the impact of these parameters generally appears to be similar in different aerosol types [7,29]. Therefore, in this section, we test the changes in ALH information under different aerosol optical depth conditions (AOD is from 0.2 to 1.0) and scale height conditions including near- ground aerosols and transported aerosols above the boundary layer (H is from 1 km to 5 km) for the vegetation surface. At the same time, combined with the corresponding posterior error, the improvements in the information quantity and posterior error after adding polarization measurements under different aerosol conditions are analyzed.

Figure 7a,b shows the variation in the DFS for the parameter H for ten typical aerosol models used in China with the aerosol condition (AOD, H) used for the intensity measurements. The figure is presented in the form of a box plot. Figure 7c,d corresponds to the

DFS after adding polarization measurements, and the other parameters are the same as those used in Figure 7a,b. When the AOD varies from 0.2 to 1.0, each box in Figure 7a–f depicts the DFS and the uncertainty reduction of ALH. On each box, the median value (solid line in the box), maximum value (whisker top), and minimum value (whisker bottom) correspond to AOD values of 0.6, 1.0, and 0.2, respectively. Figure 7e,f represents to extent to which uncertainty reduction might be improved by including polarization measurements by comparing the reduction in posterior uncertainties of H for intensity measurements with the addition of polarization measurements. The uncertainty reduction is similar to the percentage of prior error assumed in the prior error covariance matrix, which is discussed in Section 3.2.3. In this way, we can evaluate the improvement achieved by adding polarization measurements. For Figure 7, we conclude the following:

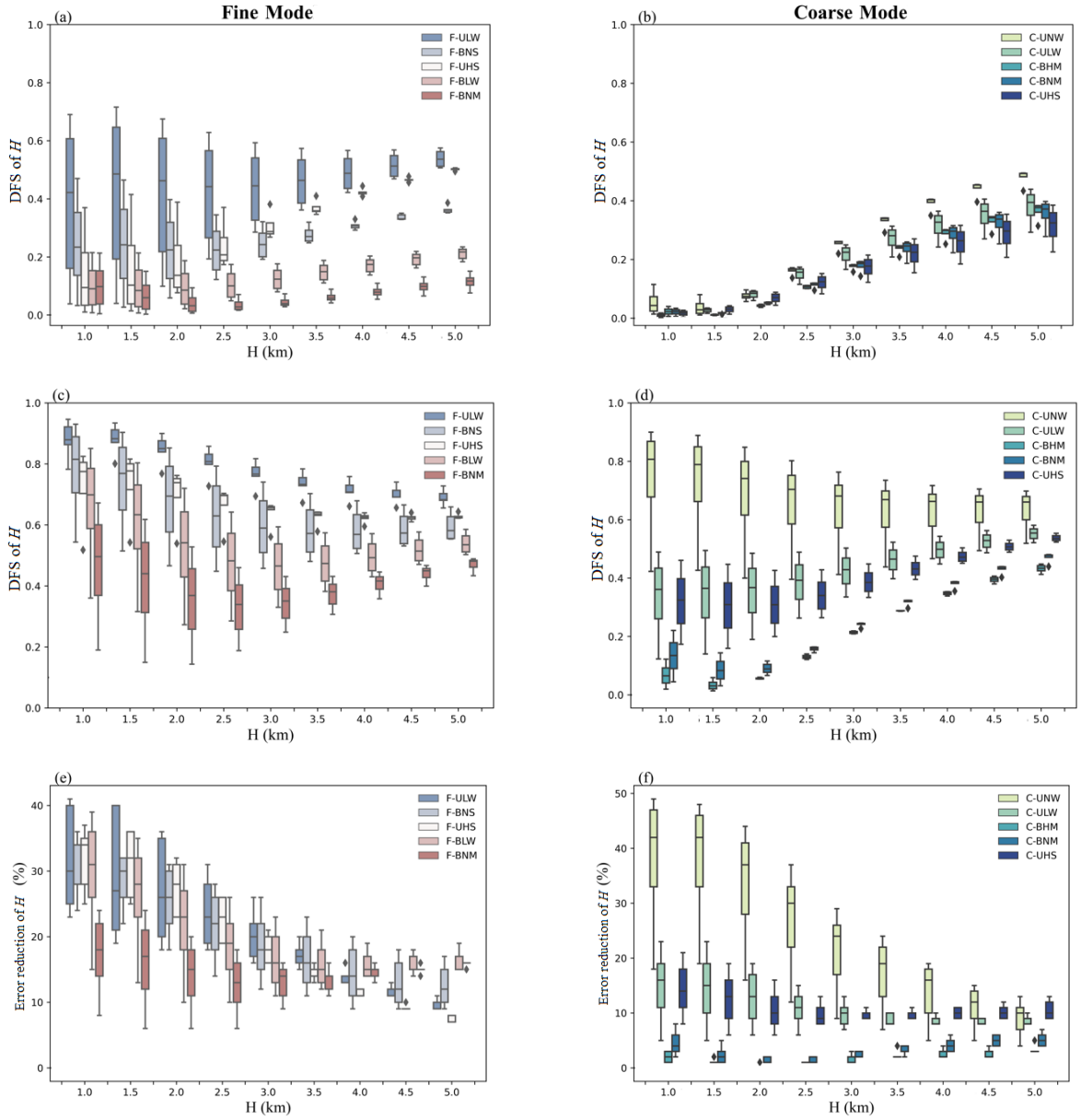

Figure 7. The DFS of H from multi-angle radiance measurements (**a**,b) and adding DoLP measurements (**c**,**d**), as well as the posterior error uncertainty reduction between these two types measurements (**e**,**f**) under different aerosol conditions for ten aerosol models over vegetation surface. (**a**,**c**,**e**) represent fine mode aerosol types and (**b**,**d**,**f**) represent coarse mode aerosol types.

(1) Comparing Figure 7a–d, it can be seen that no matter which aerosol model is used, the DFS of ALH increases at larger AOD values. For the intensity measurements, the DFS increases gradually with the increase in H. After adding the polarization measurements, the DFS gradually decreases, but the overall value is much higher than that of the intensity measurements. The polarization especially improves the ALH retrieval when the prior setting of the scale height is less than 3 km. At the same time, the difference between aerosol models has a greater impact on DFS than the changes in AOD and H, which is especially obvious for the coarse modal aerosol types.
(2) As shown in Figure 7e,f, the influence of polarization measurements on ALH retrieval gradually decreases. This is because the troposphere contains more height information, and the detection accuracy of the aerosol height is relatively high in this range. As *H* increases, the enhancement effect of polarization gradually weakens. Similar to the study presented in [33], DoLP measurements increase the sensitivity to H, and polarization multi-angle observations offer a high potential for ALH detection, but the polarization improvement shows obvious differences between aerosol models.
(3) The comparison of different models shows that the difference between the fine-mode aerosol types is small, while the difference is generally higher than that for the coarse mode aerosols. The ALH retrieval uncertainty can be reduced by 10%–39% at most through the addition of polarized measurements for F-ULW, but it can only be reduced by 6%–24% for F-BNM. In contrast, the differences among the coarse mode aerosol types affected by polarization are large. For instance, when the scale height is 1 km, the uncertainty reduction might change by as much as 49%, but the H retrieval uncertainty will only be reduced by 1%–5% (1%–8%) for C-BHM(C-BNM). It can be seen that the polarization enhancement effect is very limited for the above two coarse mode aerosol types with a moderate particle radius and weak absorption in the UV band.

5.2. The Influence of Multi-Angle Measurements

The scattering angle determined by the satellite observation geometry often determines the Rayleigh scattering and aerosol scattering, which has an important impact on ALH retrieval. Based on multi-angle satellite observations, it should be determined whether the height information obtained by the number of observation angles is sufficient for ALH retrieval. To explore the ALH inversion potential corresponding to polarization multi-angle measurements when the number of observation angles is further increased from 1 to 14, detailed geometric parameters are shown in Table A1. In Section 4.2, Figure 8 shows that even with multi-angle observations such as MAPMU with five viewing angles, it is difficult to retrieve ALH information using only intensity measurements in the UV band (DFS < 0.5). Therefore, in this section, following the addition of the polarization measurements, we examine how the DFS of ALH depends on the quantity of the observation angles to analyze whether increasing the observation angle can improve the ALH retrieval, particularly for coarse mode aerosols (C-BHM and C-BNM). When the retrieval involves multi-angle observations, the angles are selected according to the quantification of the intensity measurements with H using the Jacobian matrix from the highest (sub-satellite point) to the lowest values. Through this method, we get the following conclusions:

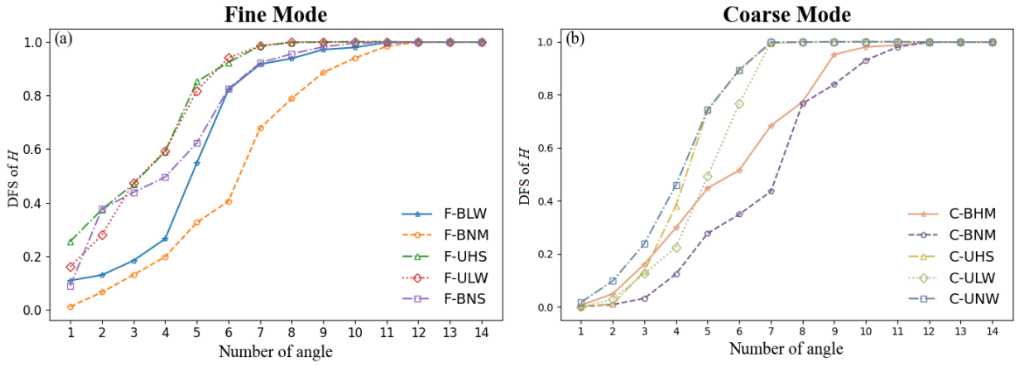

Figure 8. The DFS of H as a function of number of viewing angles for different aerosol models with AOD = 0.6 for the two aerosol types. The scale height is defined as 2 km. (**a**) represents fine mode aerosol types and (**b**) represents coarse mode aerosol types.

(1) Figure 8a,b show that the increase in the DFS with the angle number in fine mode is larger than that in coarse mode. When the angle number is 1, even in the F-UHS type with the highest DFS for fine mode, the value is only 0.28. Combined with the single-angle observation presented in Figure 9, it can be seen that, under the same conditions, when the scattering angle is around 90° and F-UHS is 120–150°, the DFS can approach 0.5. In that case, the use of single-angle polarization measurements to retrieve ALH is often limited, so the development of multi-angle polarization sensors has great significance for ALH retrieval in the UV band.

(2) In addition, given the constrained observation period in the actual multi-angle observation mode, if numerous angles focus on the same object, the target's spatial coverage or the overall number of targets will be decreased [29]. Therefore, it is necessary to find the optimal number of angles to reduce the observation time of each target while maintaining a high level of ALH information. It can be seen that, as the observation angle increases, the increase in DFS gradually decreases, but as the number of observation angles rises from 1 to 5, it basically meets the requirements of ALH retrieval (DFS > 0.5) for the main aerosol models. Even for the two aerosol types with limited polarization enhancement, C-BNM and C-BHM, the DFS is significantly improved when the observation angles increased to about 7–8. This also shows that the multi-angle observation is an effective way to improve the ALH retrieval of weak absorbing aerosol types at the UV band.

(3) As the observation angle continues to increase, the DFS increase gradually slows down with the number of angles and finally converges, which means that as the number of angles continues to increase, the inversion framework constructed in this study is easily extensible. In a future study, we will add to and evaluate the potential for retrieving more aerosol properties from the UV band through the addition of multi-angle measurements.

In order to analyze the upper limit of ALH information of single-angle polarization observations, we simulated two typical observation geometries (solar zenith angles of 40° and 60°, respectively), and there were 25 observation angles in each group. The scattering angle varied from 60° to 140° with a step size of 5°. By using the same parameter settings as before in the forward simulation, we found that for the single-angle polarization observation, the mean value between two typical observation geometries of DFS as a function of the scattering angle is as shown in Figure 9:

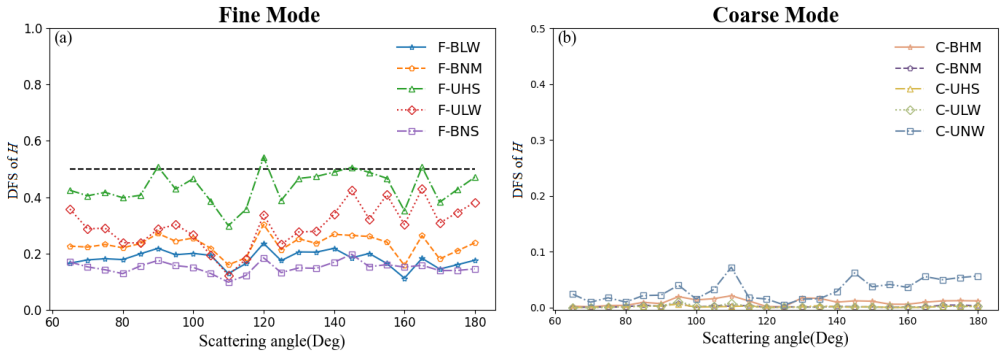

Figure 9. The DFS of *H* as a function of the scattering angle with single-angle polarization observations. (**a**) represents fine aerosol model types and (**b**) represents coarse aerosol model types.

5.3. The Influence of Model Errors

We also needed to quantitatively investigate the influence of predefined model errors on the retrieval results of ALH, because the predefined aerosol model will inevitably introduce model errors into the retrieval of critical aerosol and surface parameters in our inversion framework. Using Equation (15), we used the specified constant measurement errors from the previous section to calculate the DFS results resulting from various model errors. Previous research has shown that the DFS of the aerosol layer height will be affected by the aerosol types and has shown the differences, but the impact of AOD generally appear similar in different aerosol types [7,29]. Therefore, we concentrated on AOD = 0.6 and scale height = 2 km as a demonstration. Additionally, we have given an example of AOD = 0.2 in Figure A1 as a comparison. It was assumed that all aerosol and surface parameters change from 5% to 100%, as defined in Section 3.2.3 It was found that for both fine mode and coarse aerosol types, the DFS of ALH decreases with an increase in the parameter error, but the influence of each parameter is not the same, as shown in Figures 10 and 11. We obtained the following conclusions:

(1) For aerosol model parameters, the F-ULW and F-UHS aerosol types, the total aerosol volume, and the effective radius have the greatest influences, and decreases in DFS are all above 0.3. For the other three fine particle aerosol types, although the real part of the complex refractive index is an important factor that affects the scattering, the difference in DFS caused by the change of aerosol parameters is controlled within 0.1 (Figure 10). However, for the five coarse mode aerosol types, the influence of the total aerosol volume and the imaginary part of refractive index on the DFS occupies the main role (Figure 11).

(2) Similarly, for fine-mode aerosol types, the error of k_1 of surface parameters has the greatest influence on the DFS of ALH retrieval. In coarse mode, the DFS is much more affected by the surface BRDF ρ_s error than the other two parameters.

(3) When combined, the aerosol model coappearance probability is greater than 5% (F-ULW, F-UHS, F-BLW, C-BHM, C-UHS and C-ULW). For the ten typical aerosol models used in China, an iteration procedure among several predefined typical aerosol models has been designed to further decrease the probability of choosing a very bad value for the actual retrieval, and priority should be given to reducing the retrieval errors of three key parameters: the aerosol volume column concentration, effective variance, and imaginary part of the refractive index in the aerosol model, as well as the surface BRDF ρ_s and k_1 parameters will effectively improve the DFS of the aerosol retrieval in the UV band.

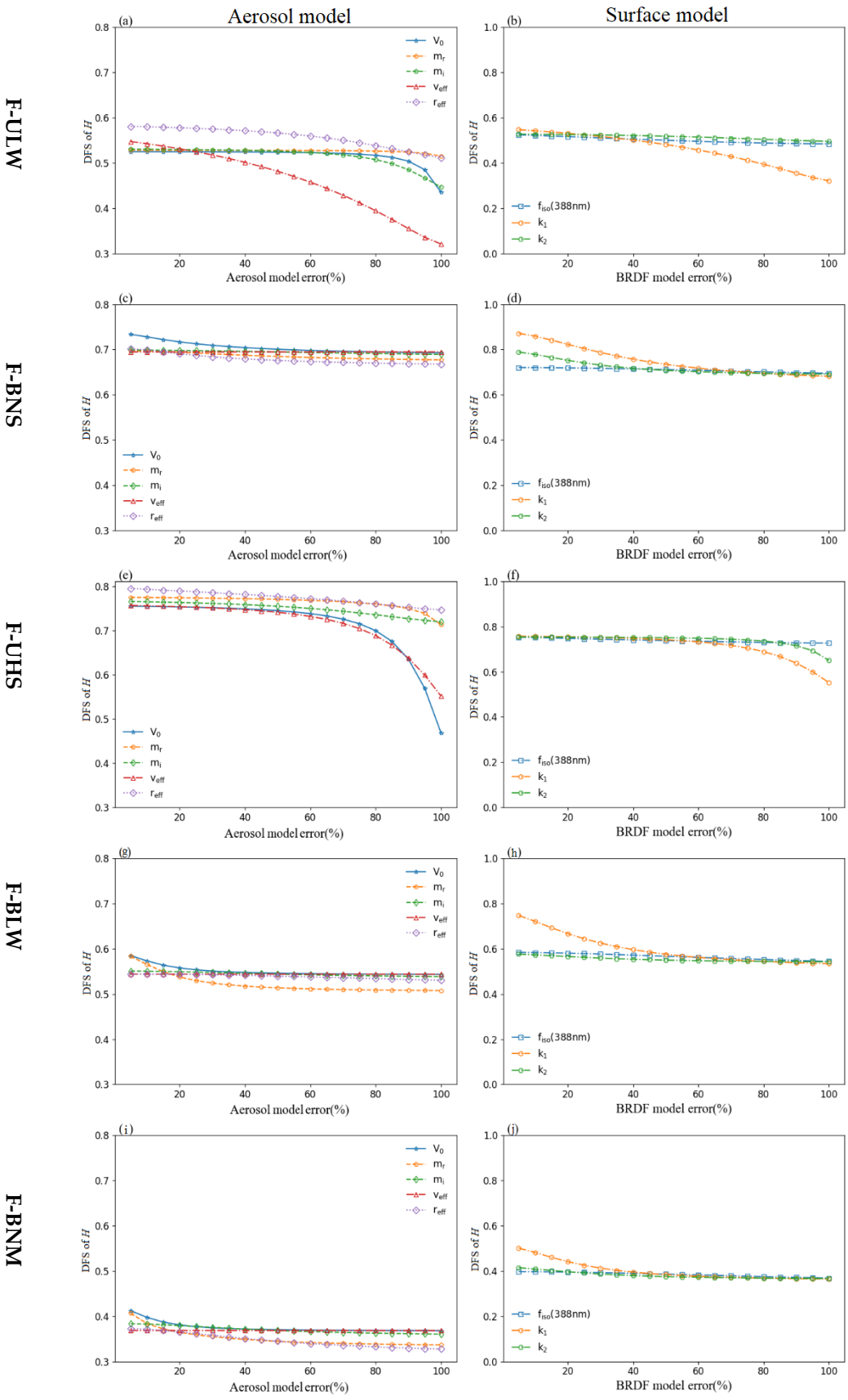

Figure 10. DFS of H as a function of the fine aerosol model and surface model parameter errors from 5% to 100% in steps of 5% with AOD = 0.6, in which left (**a**,**c**,**e**,**g**,**i**) and right panel (**b**,**d**,**f**,**h**,**j**) corresponds to the aerosol model and surface model respectively.

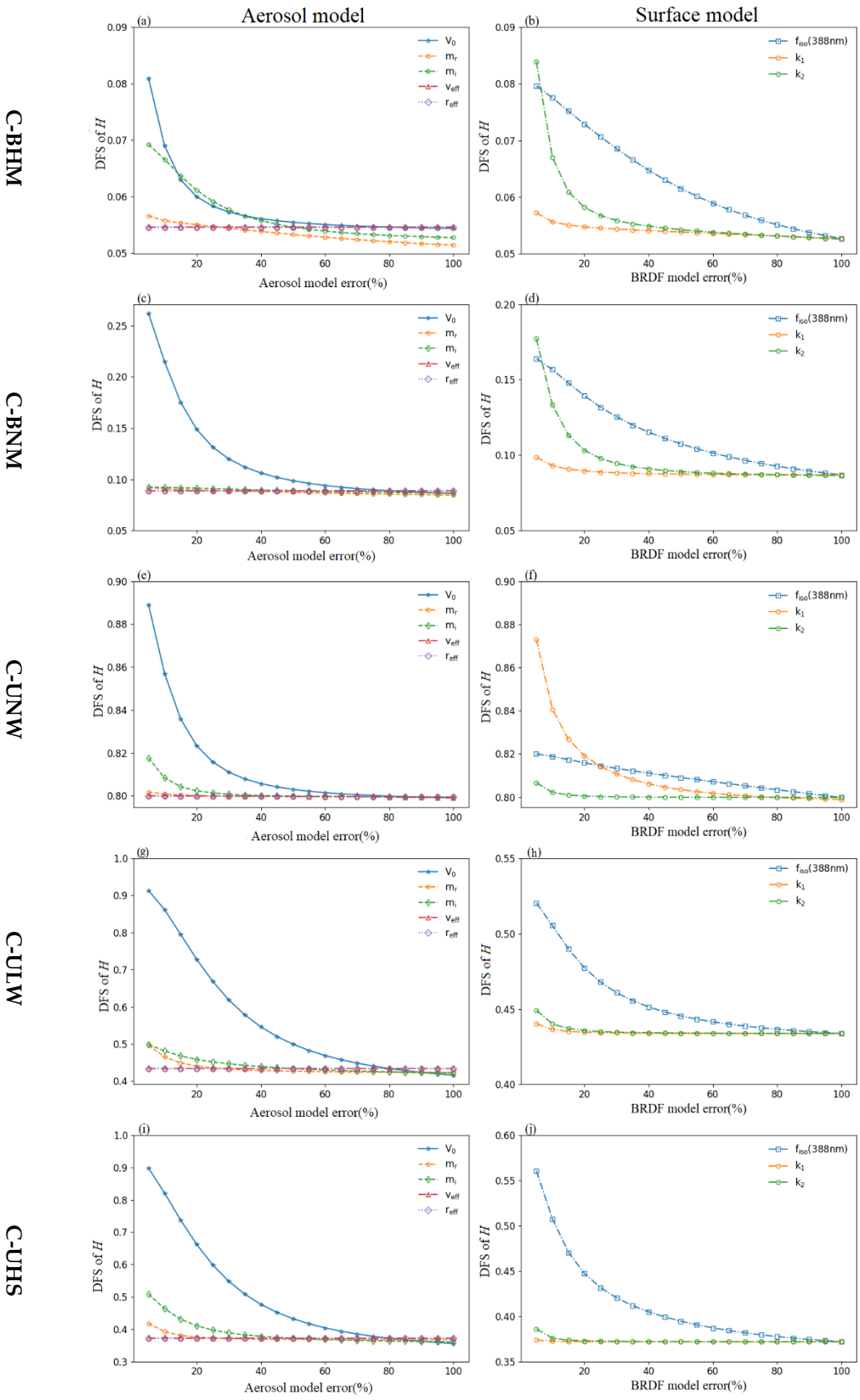

Figure 11. The same as Figure 10, but DFS of H as a function of the coarse aerosol model and surface model parameter errors from 5% to 100% in steps of 5% with AOD = 0.6, in which left (**a**,**c**,**e**,**g**,**i**) and right panel (**b**,**d**,**f**,**h**,**j**) corresponds to the aerosol model and surface model respectively.

6. Conclusions

In this paper, we used the extended ultraviolet band (388nm) to simulate multi-angle polarization synthetic data and fully evaluate the performance of multi-angle polarization measurements in the UV channel for passive remote sensing of the aerosol layer heights of ten typical aerosol model types used in the Chinese region. The research results show that

(1) The extended ultraviolet 388 nm band is an important information source for passive remote sensing ALH retrieval. With additional constraints, such as the aerosol single scattering albedo and AOD from independent sources (thought to be obtained by retrieval from other channels), MAPMU can theoretically retrieve ALH under different conditions by combining polarization measurements with multi-angle measurements.

(2) Polarization measurements have important impacts on ALH retrieval at the UV band, but the improvement is different for each typical aerosol model due to their different optical properties. For example, the reduction in posterior uncertainties of ALH retrieval is 6%–39% for the fine mode aerosol types following the addition of polarization measurements. However, the improvement for coarse mode aerosol types is relatively small, especially for C-BHM and C-BNM which characterize the types of dust found in North China and have larger median radii and low absorption rates in the UV band. The retrieved reduction of posterior uncertainties is only 1%–8%.

(3) Compared with single-angle polarization observations, which have difficulty retrieving the ALH for coarse mode aerosol types, the multi-angle observation mode effectively improves the DFS of ALH retrieval. In particular, for the ALH retrieval of C-BHM and C-BNM, the combination of polarization and multi-angle measurements could be used to improve the aerosol layer height information. When the number of viewing angles is increased to 6, the DFS increment is above 0.4, on average, for different aerosol types.

(4) The predefined model errors include the error of the total aerosol volume and the effective radius and the imaginary part of the complex refractive index as well as the error of the surface reflectivity ρ_s and the k_1 parameter, which will lead to the largest change in the DFS of ALH retrieval. The effect of other parameter errors on the aerosol and surface models is relatively small.

In summary, the addition of polarization and multi-angle measurements can effectively improve ALH retrieval compared with single-angle intensity measurements in the UV band. For ALH retrieval under coarse-mode aerosol types, in addition to considering the polarization channel, multi-angle observations also need to be considered. We suggest that the number of viewing angles should be 5–6 to achieve a good level of performance (DFS > 0.5) for ALH retrieval in the UV band for the typical aerosol model types. Additionally, reducing the retrieval errors of these key parameters, as presented above, will effectively improve the uncertainty associated with ALH retrieval in the UV band.

Author Contributions: Conceptualization, Y.Z., Z.L. (Zhengqiang Li) and W.H.; Formal analysis, H.G., Z.L. (Zhengqiang Li), W.H. and C.F.; Methodology, H.G., Z.L. (Zhenhai Liu), J.M. and C.F.; Supervision, C.F. and Z.L. (Zhengqiang Li); Visualization, H.G., Y.Z., Y.X. and L.Z. (Zhenhai Liu); Writing—original draft, H.G.; Writing—review and editing, H.G., C.F. and H.X. All authors have read and agreed to the published version of the manuscript.

Funding: This study was supported by the National Natural Science Foundation of China (Grant No. 41871269), the Major Projects of High Resolution Earth Observation Systems of National Science and Technology (05-Y30B01-9001-19/20-3), the National Outstanding Youth Foundation of China (Grant No. 41925019), and the Space Pre-research Projects (No. D010206).

Data Availability Statement: Not applicable.

Acknowledgments: We acknowledge the work of Zhu Jun of DFH Satellite Co. Ltd. and Hong Jin and Qiu Zhenwei of the Hefei Institutes of Physical Science, Chinese Academy of Sciences who were

involved with the design of the new instrument. In addition, we thank the Fine Mechanics Unified Linearized Vector Radiative Transfer Model UNL-VRTM (www.unl-vrtm.org (accessed on 6 January 2022)) developed by Jun Wang of The University of Iowa and Xiaoguang Xu of the University of Maryland, Baltimore County for their technical support. Meanwhile, thanks to the reviewers and editor for their helpful comments.

Conflicts of Interest: The authors declare no conflict of interest.

Appendix A

Table A1. Multi-viewing observation geometries for forward simulations (corresponding to Figure 8).

Number	Geometry 1	Geometry 2	Geometry 3	Geometry 4
NO. 1	[54.12, 64.09, 30.44]	[32.8,59.78,104.02]	[53.08,57.8,88.40]	[77.63,61.87,34.08]
NO. 2	[54.17,60.77, 26.19]	[32.86,55.18,106.99]	[53.13,52.95,92.08]	[77.67,57.78,30.81]
NO. 3	[54.22,57.20, 20.87]	[32.92,49.86,111.05]	[53.18,47.42,97.15]	[77.72,53.14,26.5]
NO. 4	[54.27, 53.52, 14.19]	[32.98,43.81,116.83]	[53.23,41.29,104.48]	[77.76,47.98,20.64]
NO. 5	[54.33, 49.95, 5.78]	[33.04,37.22,125.53]	[53.28,34.99,115.55]	[77.80,42.47,12.4]
NO. 6	[54.38, 46.90, 355.42]	[33.10,30.78,139.24]	[53.33,29.63,132.40]	[77.85,37.15,0.65]
NO. 7	[54.43, 44.89, 343.23]	[33.16,26.16,160.34]	[53.38,27.11,155.45]	[77.89,33.09,344.34]
NO. 8	[54.48, 44.39, 330.03]	[33.22,25.59,186.76]	[53.43,28.80,179.32]	[77.94,31.67,324.35]
NO. 9	[54.53, 45.52, 317.10]	[33.28,29.43,209.63]	[53.48,33.72,197.55]	[77.90,33.52,304.71]
NO. 10	[54.58, 47.99, 305.6]	[33.34,35.61,224.89]	[53.53,39.92,209.64]	[78.03,37.83,289.07]
NO. 11	[54.63, 51.28, 296.03]	[33.4,42.23,234.53]	[53.58,46.11,217.59]	[78.08,43.20,277.9]
NO. 12	[54.69,54.92,288.36]	[33.47,48.42,240.86]	[53.64,51.76,223.04]	[78.12,48.65,270.06]
NO. 13	[54.74,58.56,282.26]	[33.53,53.89,245.23]	[53.69,56.74,226.94]	[78.17,53.73,264.45]
NO. 14	[54.79,62.01,277.41]	[33.59,58.64248.41]	[53.74,61.06,229.85]	[78.21,59.06,257.35]

The three parameters in parentheses [] represent the solar zenith range (Deg), viewing zenith range (Deg) and relative azimuth range (Deg), respectively.

Appendix B

Equation A1 uncertainties of satellite measurement matrices ($\boldsymbol{S}_y$)

$$\boldsymbol{S}_y = \begin{bmatrix} (\varepsilon_1)^2, & c1\times\varepsilon_1\varepsilon_2, & c2\times\varepsilon_2\varepsilon_3, & c3\times\varepsilon_1\varepsilon_4, & c4\times\varepsilon_1\varepsilon_5 & & & & & \\ c1\times\varepsilon_1\varepsilon_2, & (\varepsilon_2)^2, & c5\times\varepsilon_2\varepsilon_3, & c6\times\varepsilon_2\varepsilon_4, & c7\times\varepsilon_2\varepsilon_5 & & & & & \\ c2\times\varepsilon_2\varepsilon_3, & c5\times\varepsilon_2\varepsilon_3, & (\varepsilon_3)^2, & c8\times\varepsilon_3\varepsilon_4, & c9\times\varepsilon_3\varepsilon_5 & & & 0 & & \\ c3\times\varepsilon_1\varepsilon_4, & c6\times\varepsilon_2\varepsilon_4, & c8\times\varepsilon_3\varepsilon_4, & (\varepsilon_4)^2, & c10\times\varepsilon_4\varepsilon_5 & & & & & \\ c4\times\varepsilon_1\varepsilon_5, & c7\times\varepsilon_2\varepsilon_5, & c9\times\varepsilon_3\varepsilon_5, & c10\times\varepsilon_4\varepsilon_5, & (\varepsilon_5)^2 & & & & & \\ & & & & & (\varepsilon_6)^2, & c11\times\varepsilon_6\varepsilon_7, & c12\times\varepsilon_6\varepsilon_8, & c13\times\varepsilon_6\varepsilon_9, & c14\times\varepsilon_6\varepsilon_{10} \\ & & & & & c11\times\varepsilon_6\varepsilon_7, & (\varepsilon_7)^2, & c15\times\varepsilon_7\varepsilon_8, & c16\times\varepsilon_7\varepsilon_9, & c17\times\varepsilon_7\varepsilon_{10} \\ & & 0 & & & c12\times\varepsilon_6\varepsilon_8, & c15\times\varepsilon_7\varepsilon_8, & (\varepsilon_8)^2, & c18\times\varepsilon_8\varepsilon_9, & c19\times\varepsilon_8\varepsilon_{10} \\ & & & & & c13\times\varepsilon_6\varepsilon_9, & c16\times\varepsilon_7\varepsilon_9, & c8\times\varepsilon_3\varepsilon_4, & (\varepsilon_9)^2, & c20\times\varepsilon_9\varepsilon_{10} \\ & & & & & c14\times\varepsilon_6\varepsilon_{10}, & c17\times\varepsilon_7\varepsilon_{10}, & c19\times\varepsilon_8\varepsilon_{10}, & c20\times\varepsilon_9\varepsilon_{20}, & (\varepsilon_{10})^2 \end{bmatrix} \quad \text{(A1)}$$

Combined with statistical data, c1~c20 refer to the measurement correlation coefficients between different observation angles. ε_1–ε_{10} correspond to the intensity and polarization measurement errors between the five observation angles for each multi-viewing observation.

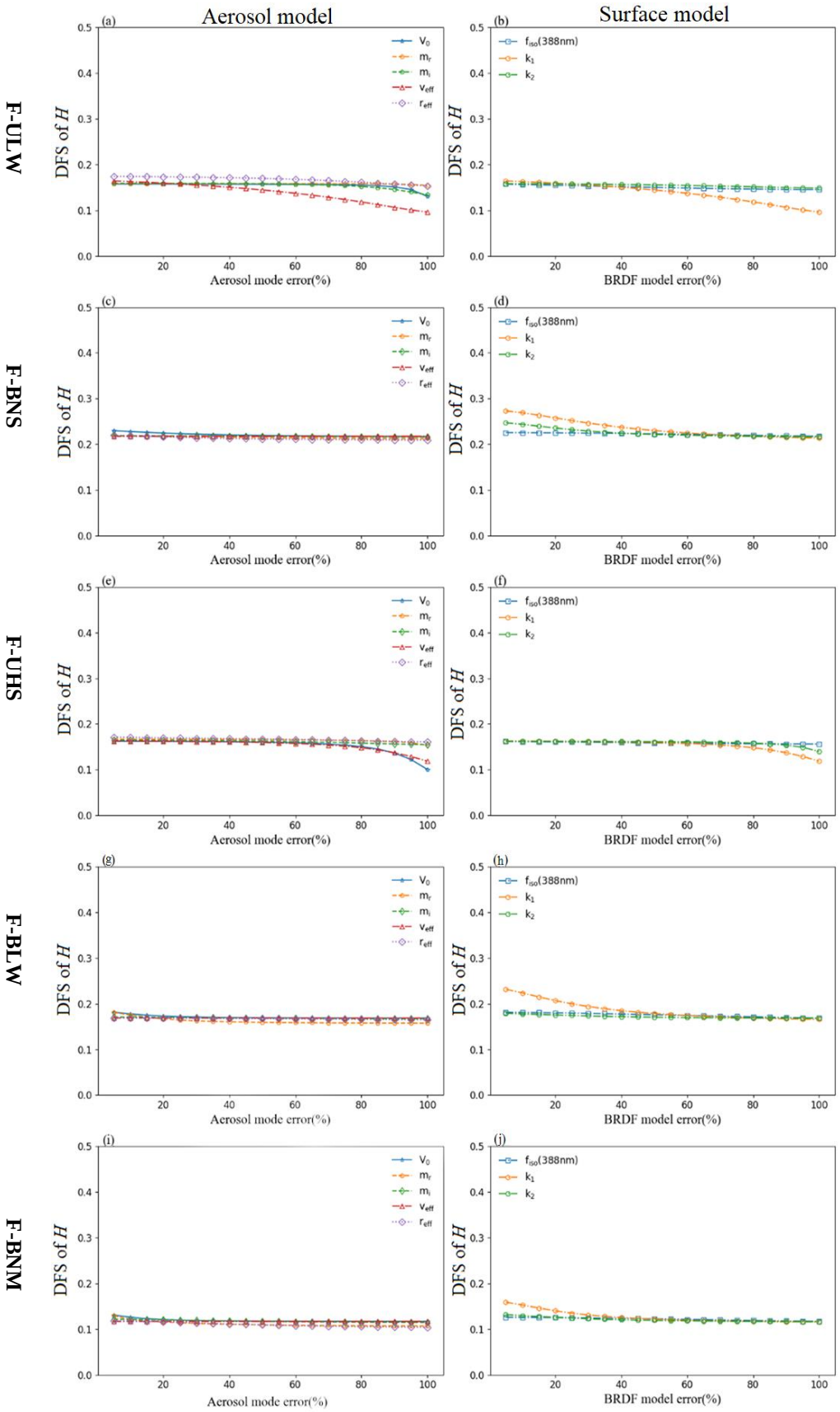

Figure A1. DFS of H as a function of the fine aerosol model and surface model parameter errors from 5% to 100% in steps of 5% but with AOD = 0.2, in which left (a,c,e,g,i) and right panel (b,d,f,h,j) corresponds to the aerosol model and surface model respectively.

References

1. Mishra, A.K.; Koren, I.; Rudich, Y. Effect of Aerosol Vertical Distribution on Aerosol-Radiation Interaction: A Theoretical Prospect. *Heliyon* **2015**, *1*, e00036. https://doi.org/10.1016/j.heliyon.2015.e00036.
2. Gordon, H.R. Atmospheric Correction of Ocean Color Imagery in the Earth Observing System Era. *J. Geophys. Res.* **1997**, *102*, 17081–17106. https://doi.org/10.1029/96JD02443.
3. Duforêt, L.; Frouin, R.; Dubuisson, P. Importance and Estimation of Aerosol Vertical Structure in Satellite Ocean-Color Remote Sensing. *Appl. Opt.* **2007**, *46*, 1107. https://doi.org/10.1364/AO.46.001107.
4. Butz, A.; Guerlet, S.; Hasekamp, O.; Schepers, D.; Galli, A.; Aben, I.; Frankenberg, C.; Hartmann, J.-M.; Tran, H.; Kuze, A.; et al. Toward Accurate CO 2 and CH 4 Observations from GOSAT: GOSAT CO 2 AND CH 4 VALIDATION. *Geophys. Res. Lett.* **2011**, *38*, n/a-n/a. https://doi.org/10.1029/2011GL047888.
5. Zhang, Y.; Li, Z. Remote Sensing of Atmospheric Fine Particulate Matter (PM2.5) Mass Concentration near the Ground from Satellite Observation. *Remote Sens. Environ.* **2015**, *160*, 252–262. https://doi.org/10.1016/j.rse.2015.02.005.
6. Wang, H.; Li, Z.; Lv, Y.; Xu, H.; Li, K.; Li, D.; Hou, W.; Zheng, F.; Wei, Y.; Ge, B. Observational Study of Aerosol-Induced Impact on Planetary Boundary Layer Based on Lidar and Sunphotometer in Beijing. *Environ. Pollut.* **2019**, *252*, 897–906. https://doi.org/10.1016/j.envpol.2019.05.070.
7. Hou, W.Z.; Wang, H.F.; Li, Z.Q.; Qie, L.L.; Ge, B.Y.; Fan, C.; Li, S. PRELIMINARY SENSITIVITY STUDY OF AEROSOL LAYER HEIGHT FROM SYNTHETIC MULTIANGLE POLARIMETRIC REMOTE SENSING MEASUREMENTS. *Int. Arch. Photogramm. Remote Sens. Spat. Inf. Sci.* **2019**, *XLII-3/W9*, 63–69. https://doi.org/10.5194/isprs-archives-XLII-3-W9-63-2019.
8. Kahn, R.A.; Chen, Y.; Nelson, D.L.; Leung, F.-Y.; Li, Q.; Diner, D.J.; Logan, J.A. Wildfire Smoke Injection Heights: Two Perspectives from Space. *Geophys. Res. Lett.* **2008**, *35*, L04809. https://doi.org/10.1029/2007GL032165.
9. Yang, Z.; Wang, J.; Ichoku, C.; Hyer, E.; Zeng, J. Mesoscale Modeling and Satellite Observation of Transport and Mixing of Smoke and Dust Particles over Northern Sub-Saharan African Region: DUST AND SMOKE MIXING OVER SAHEL. *J. Geophys. Res. Atmos.* **2013**, *118*, 12,139–12,157. https://doi.org/10.1002/2013JD020644.
10. Wu, L.; Hasekamp, O.; van Diedenhoven, B.; Cairns, B.; Yorks, J.E.; Chowdhary, J. Passive Remote Sensing of Aerosol Layer Height Using Near-UV Multiangle Polarization Measurements. *Geophys. Res. Lett.* **2016**, *43*, 8783–8790. https://doi.org/10.1002/2016GL069848.
11. Yu, H.; Chin, M.; Winker, D.M.; Omar, A.H.; Liu, Z.; Kittaka, C.; Diehl, T. Global View of Aerosol Vertical Distributions from CALIPSO Lidar Measurements and GOCART Simulations: Regional and Seasonal Variations. *J. Geophys. Res.* **2010**, *115*, D00H30. https://doi.org/10.1029/2009JD013364.
12. Winker, D.M.; Vaughan, M.A.; Omar, A.; Hu, Y.; Powell, K.A.; Liu, Z.; Hunt, W.H.; Young, S.A. Overview of the CALIPSO Mission and CALIOP Data Processing Algorithms. *J. Atmos. Ocean. Technol.* **2009**, *26*, 2310–2323. https://doi.org/10.1175/2009JTECHA1281.1.
13. Zeng, J.; Han, Q.; Wang, J. High-Spectral Resolution Simulation of Polarization of Skylight: Sensitivity to Aerosol Vertical Profile. *Geophys. Res. Lett.* **2008**, *35*, L20801. https://doi.org/10.1029/2008GL035645.
14. Chen, X.; Wang, J.; Xu, X.; Zhou, M.; Zhang, H.; Castro Garcia, L.; Colarco, P.R.; Janz, S.J.; Yorks, J.; McGill, M.; et al. First Retrieval of Absorbing Aerosol Height over Dark Target Using TROPOMI Oxygen B Band: Algorithm Development and Application for Surface Particulate Matter Estimates. *Remote Sens. Environ.* **2021**, *265*, 112674. https://doi.org/10.1016/j.rse.2021.112674.
15. Fisher, D.; Muller, J.-P.; Yershov, V.N. Automated Stereo Retrieval of Smoke Plume Injection Heights and Retrieval of Smoke Plume Masks From AATSR and Their Assessment With CALIPSO and MISR. *IEEE Trans. Geosci. Remote Sens.* **2014**, *52*, 1249–1258. https://doi.org/10.1109/TGRS.2013.2249073.
16. Zakšek, K.; Hort, M.; Zaletelj, J.; Langmann, B. Monitoring Volcanic Ash Cloud Top Height through Simultaneous Retrieval of Optical Data from Polar Orbiting and Geostationary Satellites. *Atmos. Chem. Phys.* **2013**, *13*, 2589–2606. https://doi.org/10.5194/acp-13-2589-2013.
17. Hasekamp, O.P.; Landgraf, J. Retrieval of Aerosol Properties over the Ocean from Multispectral Single-Viewing-Angle Measurements of Intensity and Polarization: Retrieval Approach, Information Content, and Sensitivity Study. *J. Geophys. Res.* **2005**, *110*, D20207. https://doi.org/10.1029/2005JD006212.
18. Kalashnikova, O.V.; Garay, M.J.; Davis, A.B.; Diner, D.J.; Martonchik, J.V. Sensitivity of Multi-Angle Photo-Polarimetry to Vertical Layering and Mixing of Absorbing Aerosols: Quantifying Measurement Uncertainties. *J. Quant. Spectrosc. Radiat. Transf.* **2011**, *112*, 2149–2163. https://doi.org/10.1016/j.jqsrt.2011.05.010.
19. Torres, O.; Tanskanen, A.; Veihelmann, B.; Ahn, C.; Braak, R.; Bhartia, P.K.; Veefkind, P.; Levelt, P. Aerosols and Surface UV Products from Ozone Monitoring Instrument Observations: An Overview. *J. Geophys. Res.* **2007**, *112*, D24S47. https://doi.org/10.1029/2007JD008809.
20. Lei, X.; Zhu, S.; Li, Z.; Hong, J.; Liu, Z.; Tao, F.; Zou, P.; Song, M.; Li, C. Integration Model of POSP Measurement Spatial Response Function. *Opt. Express* **2020**, *28*, 25480. https://doi.org/10.1364/OE.393897.
21. Lei, X.; Liu, Z.; Tao, F.; Hou, W.; Huang, H.; Xie, Y.; Zhao, X.; Dong, H.; Zou, P.; Song, M.; et al. Geolocation Error Estimation Method for the Wide Swath Polarized Scanning Atmospheric Corrector Onboard HJ-2 A/B Satellites. *IEEE Trans. Geosci. Remote Sens.* **2022**, *60*, 1–9. https://doi.org/10.1109/TGRS.2022.3193095.

22. Li, Z.; Xie, Y.; Hou, W.; Liu, Z.; Bai, Z.; Hong, J.; Ma, Y.; Huang, H.; Lei, X.; Sun, X.; et al. In-Orbit Test of the Polarized Scanning Atmospheric Corrector (PSAC) Onboard Chinese Environmental Protection and Disaster Monitoring Satellite Constellation HJ-2 A/B. *IEEE Trans. Geosci. Remote Sens.* **2022**, *60*, 1–17. https://doi.org/10.1109/TGRS.2022.3176978.
23. Shi, Z.; Li, Z.; Hou, W.; Mei, L.; Sun, L.; Jia, C.; Zhang, Y.; Li, K.; Xu, H.; Liu, Z.; et al. Aerosol Optical Depth Retrieval Based on Neural Network Model Using Polarized Scanning Atmospheric Corrector (PSAC) Data. *IEEE Trans. Geosci. Remote Sens.* **2022**, *60*, 1–18. https://doi.org/10.1109/TGRS.2022.3192908.
24. Ge, B.; Li, Z.; Chen, C.; Hou, W.; Xie, Y.; Zhu, S.; Qie, L.; Zhang, Y.; Li, K.; Xu, H.; et al. An Improved Aerosol Optical Depth Retrieval Algorithm for Multiangle Directional Polarimetric Camera (DPC). *Remote Sens.* **2022**, *14*, 4045. https://doi.org/10.3390/rs14164045.
25. Satheesh, S.K.; Torres, O.; Remer, L.A.; Babu, S.S.; Vinoj, V.; Eck, T.F.; Kleidman, R.G.; Holben, B.N. Improved Assessment of Aerosol Absorption Using OMI-MODIS Joint Retrieval. *J. Geophys. Res.* **2009**, *114*, D05209. https://doi.org/10.1029/2008JD011024.
26. Rodgers, C.D. *Inverse Methods For Atmospheric Sounding: Theory And Practice*; World Scientific, 2000; ISBN 978-981-4498-68-5.
27. Hou, W.; Wang, J.; Xu, X.; Reid, J.S.; Han, D. An Algorithm for Hyperspectral Remote Sensing of Aerosols: 1. Development of Theoretical Framework. *J. Quant. Spectrosc. Radiat. Transf.* **2016**, *178*, 400–415. https://doi.org/10.1016/j.jqsrt.2016.01.019.
28. Hou, W.; Wang, J.; Xu, X.; Reid, J.S. An Algorithm for Hyperspectral Remote Sensing of Aerosols: 2. Information Content Analysis for Aerosol Parameters and Principal Components of Surface Spectra. *J. Quant. Spectrosc. Radiat. Transf.* **2017**, *192*, 14–29. https://doi.org/10.1016/j.jqsrt.2017.01.041.
29. Chen, X.; Xu, X.; Wang, J.; Diner, D.J. Can Multi-Angular Polarimetric Measurements in the Oxygen-A and B Bands Improve the Retrieval of Aerosol Vertical Distribution? *J. Quant. Spectrosc. Radiat. Transf.* **2021**, *270*, 107679. https://doi.org/10.1016/j.jqsrt.2021.107679.
30. Zhu, Y.; Gelaro, R. Observation Sensitivity Calculations Using the Adjoint of the Gridpoint Statistical Interpolation (GSI) Analysis System. *Mon. Weather Rev.* **2008**, *136*, 335–351. https://doi.org/10.1175/MWR3525.1.
31. Mlawer, E.J.; Payne, V.H.; Moncet, J.-L.; Delamere, J.S.; Alvarado, M.J.; Tobin, D.C. Development and Recent Evaluation of the MT_CKD Model of Continuum Absorption. *Phil. Trans. R. Soc. A.* **2012**, *370*, 2520–2556. https://doi.org/10.1098/rsta.2011.0295.
32. Xu, X.; Wang, J. UNL-VRTM, A Testbed for Aerosol Remote Sensing: Model Developments and Applications. In *Springer Series in Light Scattering*; Kokhanovsky, A., Ed.; Springer Series in Light Scattering; Springer International Publishing: Cham, Switzerland, 2019; pp. 1–69 ISBN 978-3-030-20586-7.
33. Hess, M.; Koepke, P.; Schult, I. Optical Properties of Aerosols and Clouds: The Software Package OPAC. *Bull. Amer. Meteor. Soc.* **1998**, *79*, 831–844. https://doi.org/10.1175/1520-0477(1998)079<0831:OPOAAC>2.0.CO;2.
34. Hou, W.; Wang, J.; Xu, X.; Reid, J.S.; Janz, S.J.; Leitch, J.W. An Algorithm for Hyperspectral Remote Sensing of Aerosols: 3. Application to the GEO-TASO Data in KORUS-AQ Field Campaign. *J. Quant. Spectrosc. Radiat. Transf.* **2020**, *253*, 107161. https://doi.org/10.1016/j.jqsrt.2020.107161.
35. Li, Z.; Zhang, Y.; Xu, H.; Li, K.; Dubovik, O.; Goloub, P. The Fundamental Aerosol Models Over China Region: A Cluster Analysis of the Ground-Based Remote Sensing Measurements of Total Columnar Atmosphere. *Geophys. Res. Lett.* **2019**, *46*, 4924–4932. https://doi.org/10.1029/2019GL082056.
36. Wang, J.; Xu, X.; Ding, S.; Zeng, J.; Spurr, R.; Liu, X.; Chance, K.; Mishchenko, M. A Numerical Testbed for Remote Sensing of Aerosols, and Its Demonstration for Evaluating Retrieval Synergy from a Geostationary Satellite Constellation of GEO-CAPE and GOES-R. *J. Quant. Spectrosc. Radiat. Transf.* **2014**, *146*, 510–528. https://doi.org/10.1016/j.jqsrt.2014.03.020.
37. Li, Z.; Hou, W.; Hong, J.; Zheng, F.; Luo, D.; Wang, J.; Gu, X.; Qiao, Y. Directional Polarimetric Camera (DPC): Monitoring Aerosol Spectral Optical Properties over Land from Satellite Observation. *J. Quant. Spectrosc. Radiat. Transf.* **2018**, *218*, 21–37. https://doi.org/10.1016/j.jqsrt.2018.07.003.
38. Baldridge, A.M.; Hook, S.J.; Grove, C.I.; Rivera, G. The ASTER Spectral Library Version 2.0. *Remote Sens. Environ.* **2009**, *113*, 711–715. https://doi.org/10.1016/j.rse.2008.11.007.
39. *USGS Spectral Library Version 7*; Data Series; USGS: Reston, VA, 2017; p. P67;.
40. Litvinov, P.; Hasekamp, O.; Dubovik, O.; Cairns, B. Model for Land Surface Reflectance Treatment: Physical Derivation, Application for Bare Soil and Evaluation on Airborne and Satellite Measurements. *J. Quant. Spectrosc. Radiat. Transf.* **2012**, *113*, 2023–2039. https://doi.org/10.1016/j.jqsrt.2012.06.027.
41. Ma, Y.; Li, Z.; Li, Z.; Xie, Y.; Fu, Q.; Li, D.; Zhang, Y.; Xu, H.; Li, K. Validation of MODIS Aerosol Optical Depth Retrieval over Mountains in Central China Based on a Sun-Sky Radiometer Site of SONET. *Remote Sens.* **2016**, *8*, 111. https://doi.org/10.3390/rs8020111.
42. Li, Z.Q.; Xu, H.; Li, K.T.; Li, D.H.; Xie, Y.S.; Li, L.; Zhang, Y.; Gu, X.F.; Zhao, W.; Tian, Q.J.; et al. Comprehensive Study of Optical, Physical, Chemical, and Radiative Properties of Total Columnar Atmospheric Aerosols over China: An Overview of Sun–Sky Radiometer Observation Network (SONET) Measurements. *Bull. Am. Meteorol. Soc.* **2018**, *99*, 739–755. https://doi.org/10.1175/BAMS-D-17-0133.1.